Journal of *Marine Science and Engineering*

MDPI

Article

Near-Inertial Waves Induced by Typhoon Megi (2010) in the South China Sea

Anzhou Cao [1,2,3,*], Zheng Guo [4], Yunhe Pan [1], Jinbao Song [1], Hailun He [2] and Peiliang Li [1,5]

1 Ocean College, Zhejiang University, Zhoushan 316021, China; 18716037312@163.com (Y.P.); songjb@zju.edu.cn (J.S.); lipeiliang@zju.edu.cn (P.L.)
2 State Key Laboratory of Satellite Ocean Environment Dynamics, Second Institute of Oceanography, Ministry of Natural Resources, Hangzhou 310012, China; hehailun@sio.org.cn
3 Laboratory for Regional Oceanography and Numerical Modeling, Qingdao National Laboratory for Marine Science and Technology, Qingdao 266061, China
4 Marine Science and Technology College, Zhejiang Ocean University, Zhoushan 316022, China; guozheng-gz@163.com
5 Hainan Institution of Zhejiang University, Sanya 572025, China
* Correspondence: caoanzhou@zju.edu.cn

Abstract: Near-inertial waves (NIWs) are a kind of internal wave, which are usually generated by synoptic wind forcing and play an important role in the oceanic energy budget. However, the lack of in situ observations limits our understanding of NIWs to some extent. Through a comparison with in situ observations, in this study, we first showed that the hybrid coordinate ocean model reanalysis results could reasonably reproduce the typhoon-induced NIWs, and we then adopted these data to investigate the NIWs induced by typhoon Megi in 2010 in the South China Sea (SCS). The results indicate that Megi-induced near-inertial kinetic energy was mainly concentrated in the SCS Basin. In the vertical direction, Megi-induced NIWs could propagate to 1000 m depth. The damping and modal content of Megi-induced NIWs were site-dependent: In the region near Megi's track, NIWs were dominated by the first three baroclinic modes and damped quickly; whereas in two zones to the west of the Luzon Island and Luzon Strait, the e-folding time of Megi-induced NIWs could be longer than 20 days and higher modes (mode-4 to mode-7) were enhanced several days after the passage of Megi. Possible mechanisms of these phenomena were also explored in this study.

Keywords: near-inertial waves; typhoon Megi; South China Sea; hybrid coordinate ocean model reanalysis results

Citation: Cao, A.; Guo, Z.; Pan, Y.; Song, J.; He, H.; Li, P. Near-Inertial Waves Induced by Typhoon Megi (2010) in the South China Sea. *J. Mar. Sci. Eng.* **2021**, *9*, 440. https://doi.org/10.3390/jmse9040440

Academic Editors: Matt Lewis and SungHyun Nam

Received: 8 March 2021
Accepted: 15 April 2021
Published: 18 April 2021

1. Introduction

Near-inertial waves (NIWs) are a kind of internal wave, which are ubiquitous in the global ocean. In the internal wave spectrum, NIWs appear as a predominant peak near the local inertial frequency, and hence, act as a dominant mode of high-frequency variability in the ocean [1]. NIWs play an important role in the oceanic energy budget [2,3], as they can cause intense shear [4,5] and contribute to the elevation of turbulent mixing [6,7].

There are various mechanisms that can cause NIWs, among which, the most important is synoptic wind forcing. According to previous estimations, the global power of wind-driven near-inertial motions is 0.3–1.5 TW [8–14], which is comparable to the global power converted from astronomical tides to internal tides [3,15,16]. Due to strong wind stresses and their compact size, tropical cyclones (typhoons and hurricanes) are an efficient generator of NIWs [1]. Moreover, nonlinear wave–wave interaction, including parametric subharmonic instability [17–19] and resonant triad interaction [20–22], lee waves [23], frontal jets [24] and mesoscale eddies [25], can also induce NIWs under some conditions.

The Western North Pacific is the region with the highest concentration of typhoons in the world [26]. According to the estimation of Nguyen et al. [27], there are an average of 22 typhoons per year and most of them pass through the South China Sea (SCS), the

largest marginal sea in the Western North Pacific. The frequency of typhoons has shown an increasing trend in the SCS [28]. They import a significant amount of energy to the ocean and induce intense NIWs [29]. Several previous studies have reported typhoon-induced NIWs in the SCS through analyzing in situ observations [30–40]. However, due to the differences in typhoon characteristics, mooring-measuring ranges, distances between typhoon centers and moorings, and local conditions, the NIWs induced by different typhoons usually exhibit different features and those induced by the same typhoon are site-dependent [31,32,34,35,37]. More importantly, because of the great difficulties and large costs of in situ observations, it is nearly impossible to simultaneously deploy sufficient moorings to observe NIWs induced by the same typhoon, which limits our understanding of NIWs to some extent.

In this study, through a comparison with in situ observations, we first showed that the hybrid coordinate ocean model (HYCOM) reanalysis results could reasonably reproduce the typhoon-induced NIWs. Thereafter, these data were used to investigate the characteristics of NIWs induced by typhoon Megi in 2010, with the aim of deepening our understanding of typhoon-induced NIWs in the SCS. The paper is organized as follows. Typhoon Megi, the HYCOM reanalysis results and corresponding data analysis methods are introduced in Section 2. A comparison between the HYCOM reanalysis results and in situ observations is performed in Section 3. After validation, the HYCOM reanalysis results are used to reveal the energy and modal characteristics of Megi-induced NIWs, which are shown in Sections 4 and 5, respectively. A discussion is presented in Section 6. Finally, the conclusions of this study complete the paper in Section 7.

2. Data and Methodology

2.1. Typhoon Megi

Megi was the 15th typhoon that occurred in 2010 in the Western Pacific. It was also the strongest typhoon worldwide in 2010 [32]. According to the best track data from the China Meteorological Administration tropical cyclone database [41], Megi first formed as a tropical depression at 11.8° N, 141.4° E on 13 October. Then, it moved northwestward and enhanced rapidly. Before landing on Luzon Island on 18 October, Megi upgraded to a super typhoon. After passing Luzon Island, Megi weakened a little to a severe typhoon until 22 October. Thereafter, Megi damped quickly and finally dissipated on 24 October. The track and status of Megi in the SCS are shown in Figure 1.

2.2. Data

The HYCOM reanalysis results (GLBu0.08/expt_19.1, including surface elevation, horizontal velocities, water temperature and salinity) in the SCS from 16 October to 20 November 2010 were used to analyze the ocean dynamical response to typhoon Megi. These data have a spatial resolution of 1/12.5° and a temporal interval of 3 h, which are available from www.hycom.org/data/glbu0pt08/expt-19pt1 (accessed on 1 January 2021). The wind forcing used in the HYCOM is the 1-hourly National Centers for Environmental Prediction (NCEP) Climate Forecast System Reanalysis (CFSR) wind data, which captured typhoon Megi [37]. Additionally, note that the Navy Coupled Ocean Data Assimilation (NCODA) system was used for data assimilation when generating the reanalysis data. In addition, to validate the HYCOM reanalysis results, the bandpass filtered NIWs at mooring UIB6 (Figure 1) were used in this study, which are cited from [37].

2.3. Methodology

First of all, the HYCOM reanalysis results were compared with in situ observations at mooring UIB6 for validation. A continuous wavelet transform was first performed to demonstrate the existence of NIWs. As tidal forcing was not considered in the HYCOM reanalysis results (GLBu0.08/expt_19.1), the bandpass filtered NIWs rather than the raw currents were compared with those from in situ observations. To be consistent with previous studies [32,37], the fourth-order Butterworth filter was adopted and the cutoff

frequency of bandpass filtering was set to [0.58, 0.81] cpd corresponding to 0.80–1.13 times the local Coriolis frequency.

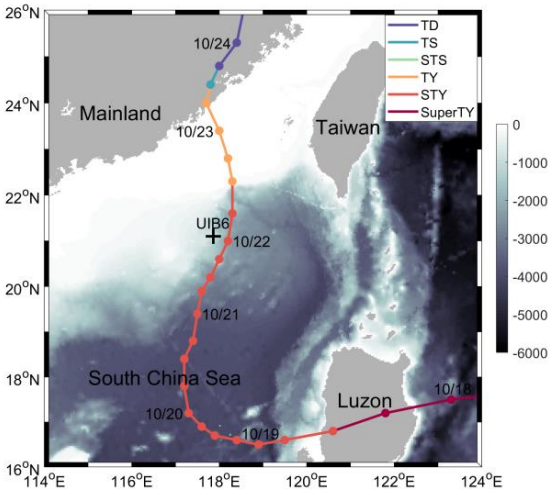

Figure 1. Bathymetry (shading, unit: m) of the northern SCS, track of typhoon Megi (colored lines) and position of mooring UIB6 (black plus). Six-hour positions of Megi's center are denoted by dots and the time at 00:00 from 19 to 24 October is labeled. Intensity of Megi is represented by various colors, as shown in the legend. TD, TS, STS, TY, STY and SuperTY are abbreviations of tropical depression (10.8–17.1 m/s), tropical storm (17.2–24.4 m/s), severe tropical storm (24.5–32.6 m/s), typhoon (32.7–41.4 m/s), severe typhoon (41.5–50.9 m/s) and super typhoon (>51.0 m/s), respectively.

After validation, the near-inertial kinetic energy density (NIKE) was calculated as:

$$\mathrm{NIKE} = \frac{1}{2}\rho_0\left(u_f^2 + v_f^2\right) \tag{1}$$

where ρ_0 = 1024 kg/m^3 is the reference density, u_f and v_f are the zonal and meridional components of the bandpass filtered NIWs, respectively [32]. In this study, we also calculated the depth-integrated NIKE to investigate the horizontal distribution of Megi-induced NIWs. Based on the depth-integrated NIKE, the e-folding time of Megi-induced NIWs was calculated to explore their decay.

To investigate the propagation of Megi-induced NIWs, we adopted the same method as [42,43] to separate the NIWs propagating in different directions. This method is based on Hilbert transform as well as filtering, Fourier transform and its inverse transform. For the time series of one-dimensional, two-dimensional and three-dimensional wave fields, this method can automatically identify waves propagating in two, four and eight directions, respectively. Refer to [42] for details of this method. In this study, we adopted this method to deal with the bandpass filtered NIWs along 118° E to explore the propagation of Megi-induced NIWs and their reflection at the continental slope of the northern SCS.

Modal content is an important characteristic of internal waves [44–48]. Therefore, it was investigated for Megi-induced NIWs in this study. For the zonal and meridional components of NIWs,

$$\begin{cases} u_f(z,t) = \sum\limits_{n=0}^{N_m} u_{fn}(t)\cdot\Pi_n(z) \\ v_f(z,t) = \sum\limits_{n=0}^{N_m} v_{fn}(t)\cdot\Pi_n(z) \end{cases} \tag{2}$$

where u_{fn} and v_{fn} are the modal components of u_f and v_f with respect to mode n (n = 0, 1, . . . , N_m, n = 0 for the barotropic mode and n > 0 for baroclinic modes), and

$$\Pi_n(z) = \rho_0 c_n^2 \frac{\mathrm{d}\Phi_n(z)}{\mathrm{d}z} \tag{3}$$

are the normal modes corresponding to velocity, where $\Phi_n(z)$ are the eigenfunctions of the eigenvalue problem for eigenspeed c_n:

$$\frac{d^2\Phi_n}{dz^2} + \frac{N^2}{c_n^2}\Phi_n = 0 \quad (4)$$

subject to boundary conditions $\Phi_n(0) = \Phi_n(-H) = 0$, where H is the water depth and N is the buoyancy frequency [45].

Based on the temperature and salinity data of the HYCOM reanalysis results, the buoyancy frequency was calculated, and hence, normal modes Φ_n and Π_n. According to [47], the time-varying stratification has little influence on the modal decomposition result. Therefore, the time-averaged temperature and salinity were used to calculate the buoyancy frequency and normal modes Φ_n and Π_n. Figure 2 shows an example at 117.04° E, 18.48° N. In theory, N_m should be infinite in modal decomposition. Whereas in practice, N_m is usually set to be a certain value that is sufficient to capture the internal wave features. Generally, according to previous studies, 3, 5 and 10 are typical values used in modal decomposition [45–48]. Additionally, note that too large N_m may cause overfitting [46]. In this study, we found that N_m = 10 could well reproduce the NIKE and did not cause overfitting. Therefore, N_m = 10 was adopted in the modal decomposition in this study.

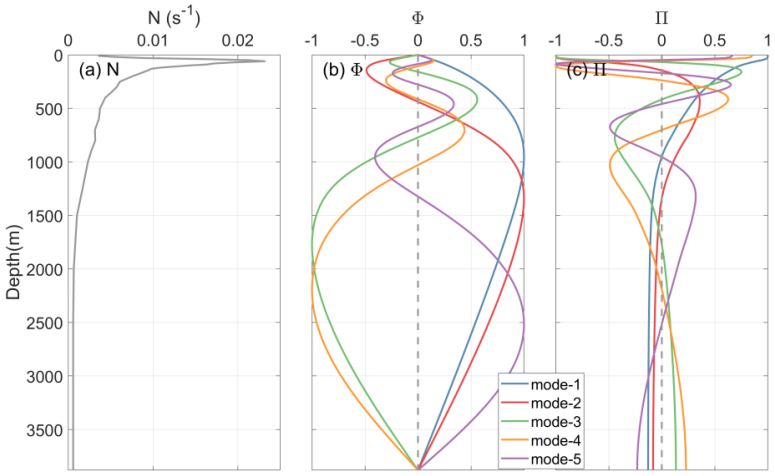

Figure 2. (**a**) Buoyancy frequency and normal modes (**b**) Φ and (**c**) Π of the first five baroclinic modes at 117.04° E, 18.48° N. Note that the normal modes shown in (**b**,**c**) have been normalized.

3. Comparison with In Situ Observations

Figure 3 displays the HYCOM zonal currents at mooring UIB6 as well as the continuous wavelet transformation of HYCOM zonal currents at 400 m depth at the mooring. It is clearly shown, that after the passage of typhoon Megi, oscillations appeared in the zonal currents. In Figure 3b, a peak exists near the local Coriolis frequency, suggesting that the oscillations in the zonal currents are Megi-induced NIWs.

Figure 4 compares the NIWs extracted from in situ observations and the HYCOM reanalysis results at mooring UIB6. Although the temporal intervals of the HYCOM reanalysis results (3 h) and observations (1 h) are different, the NIWs extracted from the HYCOM reanalysis results show a good agreement with those from observations: Both NIWs were rapidly enhanced after the passage of typhoon Megi, suggesting that they were induced by typhoon Megi; both NIWs had upward-propagating phases, suggesting that their energy was downward-propagating, which is consistent with the general features of typhoon-induced NIWs [49–51]; both NIWs were quickly damped at mooring UIB6. This result preliminarily verifies the accuracy of the HYCOM reanalysis results. To quantitatively assess the HYCOM reanalysis results, Figure 5 shows the lowpass filtered current variance of NIWs (Var $= u_f^2 + v_f^2$; [37]) averaged between 50 and 420 m depth (the effective

measuring range at UIB6; [37]) for both observations and HYCOM reanalysis results. As seen, both the HYCOM and observed current variance shows the development and decaying of Megi-induced NIWs at UIB6. The correlation coefficient between the HYCOM and observed current variance is 0.97 with a p-value much smaller than 0.01, suggesting good consistency between them. Additionally, note that the peak value of the HYCOM current variance is greater than that of the observed current variance. This is reasonable because tidal forcing was not considered in the HYCOM reanalysis results (GLBu0.08/expt_19.1); hence, nonlinear interaction between NIWs and internal tides cannot occur. As the nonlinear interaction between internal waves can transfer a significant amount of energy [52], the ignored tidal forcing in the HYCOM reanalysis results (GLBu0.08/expt_19.1) finally leads to an overestimation of the energy and current variance of NIWs. Although the HYCOM reanalysis results overestimate the intensity of NIWs, it may only have a limited influence on the distribution, decaying and modal content of NIWs, which are the main focus of this study.

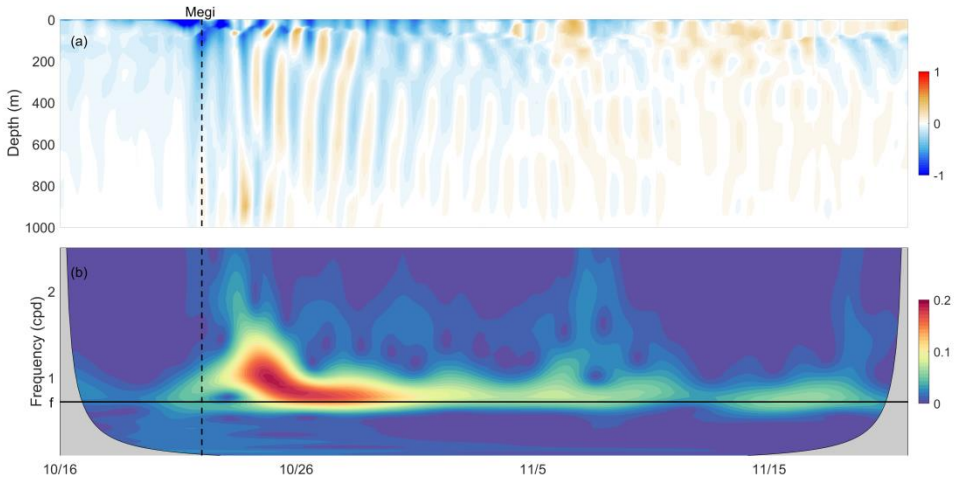

Figure 3. (**a**) HYCOM zonal currents at UIB6 (shading, unit: m/s) as a function of time and depth. (**b**) Continuous wavelet transform (shading, unit: m/s) of HYCOM zonal currents at 400 m depth at UIB6 as a function of time and frequency. The horizontal black solid line indicates the local inertial frequency. In (**a**,**b**), the vertical black dashed lines denote the time when Megi passed (00:00 on 22 October).

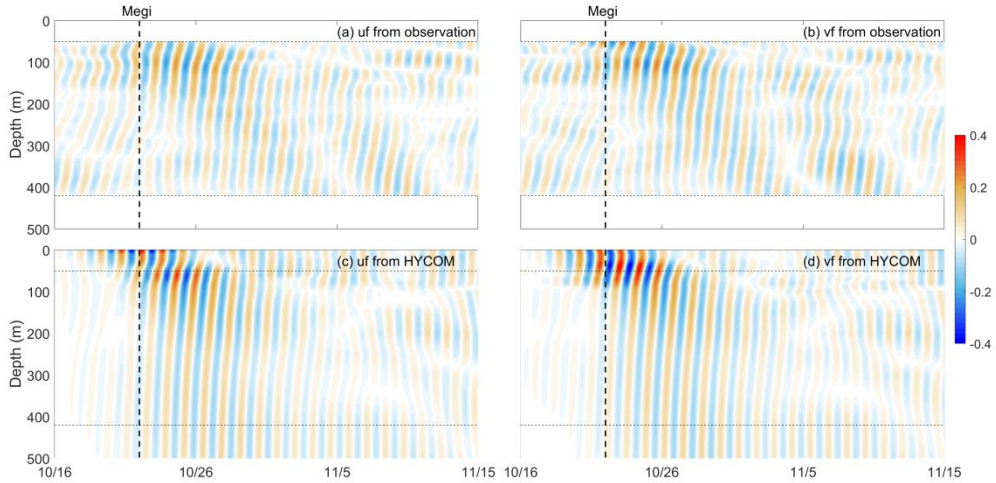

Figure 4. Comparison of (**a**,**c**) zonal and (**b**,**d**) meridional currents of NIWs (shading, unit: m/s) between (**a**,**b**) observations and (**c**,**d**) HYCOM reanalysis results at UIB6.The vertical black dashed line in each subfigure denotes the time when Megi passed (00:00 on 22 October).

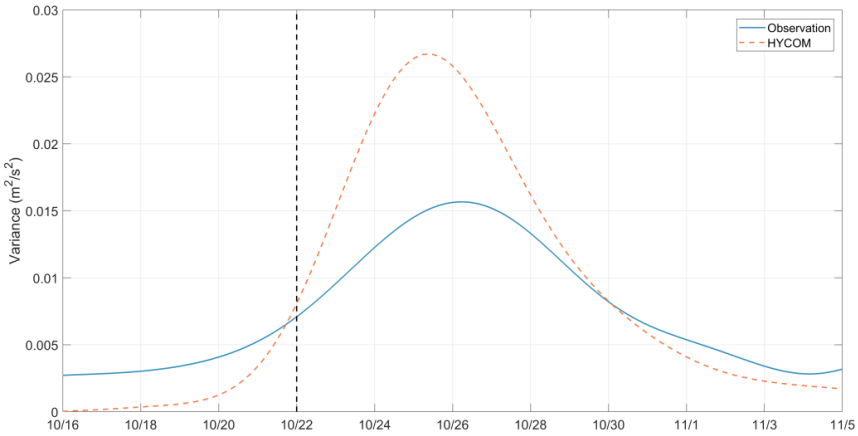

Figure 5. Comparison of lowpass filtered depth-averaged current variance of NIWs between observations (blue solid) and HYCOM reanalysis results (orange dashed) at UIB6. The vertical black dashed line indicates the time when Megi passed (00:00 on 22 October).

4. Megi-Induced NIKE

4.1. Temporal Variation and Spatial Distribution

Figure 6 illustrates the depth-integrated NIKE from 18 October to 1 November with an interval of 2 days, from which the evolution of Megi-induced NIWs is detected. At 00:00 on 18 October when Megi's center did not enter the SCS (Figure 1), slight NIKE was found to the west of Luzon Island (Figure 6a). At 00:00 on 20 October, when Megi's center was at 117.3° E, 17.2° N in the SCS, Megi-induced NIKE reached 10–20 kJ/m^2 and was mainly concentrated in two zones to the north and south of typhoon Megi, respectively (Figure 6b). From 22 to 26 October, strong NIKE with several hot spots exceeding 35 kJ/m^2 appeared along Megi's wake (Figure 6c–e). It should be noted that Megi had left the SCS Basin before 12:00 on 22 October and finally dissipated on 24 October, which means that the strongest NIKE appeared several days after the passage of Megi rather than under its influence. Thereafter, strong NIKE scattered (mainly westward propagated) and the NIKE along Megi's wake quickly damped to below 10 kJ/m^2 after 30 October (Figure 6f–h). According to [53], the ocean's response to a typhoon in the northern hemisphere usually exhibits rightward biased features, i.e., larger sea surface temperature cooling, greater currents and deeper mixed layer appear to the right of the typhoon track. As shown in Figure 6, Megi-induced NIWs also exhibited apparent rightward biased features: the NIKE to the right of Megi's wake was stronger than that to the left.

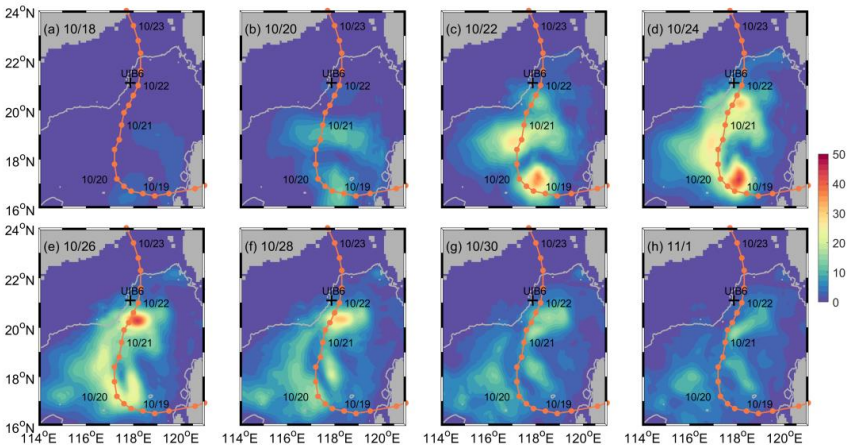

Figure 6. Depth-integrated NIKE (shading, unit: kJ/m^2) at 00:00 on (**a**) 18, (**b**) 20, (**c**) 22, (**d**) 24, (**e**) 26, (**f**) 28 and (**g**) 30 October and (**h**) 1 November 2010. Orange curves denote the track of typhoon Megi and the black plus indicates the position of mooring UIB6. The gray curve represents the 1000 m isobath.

It is interesting to find from Figure 6 that Megi-induced NIKE was mainly concentrated in the deep SCS Basin where the water depth is greater than 1000 m (the gray curve in Figure 6), although typhoon Megi passed over both the deep SCS basin and shallow continental shelf and slope in the northern SCS. To investigate the possible cause of this phenomenon, Figure 7 illustrates several snapshots of meridional currents of NIWs along 118° E on 24 October. Similar results can be found at other meridional sections on the adjacent several days. From Figure 7, we can detect that the continental slope in the northern SCS is supercritical to Megi-induced NIWs, i.e., the topographic slope (the black solid lines in Figure 7) is apparently larger than that of NIWs. In other words, the NIWs impinging on the continental slope in the northern SCS would be reflected to the SCS Basin. However, due to the complex vertical pattern of NIWs shown in Figure 7, the reflection of NIWs is not visible. Therefore, we adopted the same method as [42,43] to separate the NIWs propagating in different directions. Figure 8 shows an example at 00:00 on 24 October. The NIW component with $m > 0$ (m represents the vertical wavenumber) dominates over that with $m < 0$, suggesting that the energy of Megi-induced NIWs mainly propagated downward, which is consistent with the above analysis and general features of typhoon-induced NIWs [49–51]. For the same m, the NIW component with $l > 0$ (l represents the horizontal wavenumber) is comparable to that with $l < 0$, suggesting that the northward-propagating and southward-propagating NIWs had comparable intensity. In order to study whether Megi-induced NIWs reflected on the continental slope, attention should be paid to the northward–downward (l>0 and $m > 0$) and southward–downward ($l < 0$ and $m > 0$) components (Figure 8b,d). According to Figure 8b, two northward–downward-propagating beams impinged on the continental slope in the northern SCS, which radiated from the surface at 19–20.5° N (positive sign) and 20.5–22° N (negative sign), respectively. At the same time, two southward–downward-propagating beams were found to radiate from the continental slope with different signs (Figure 8d). To demonstrate that the two southward–downward-propagating beams are the reflected beams of the two northward–downward-propagating ones, a simple ray tracing model [54,55] is adopted to qualitatively illustrate the propagating paths of NIWs. Given that reflection occurred in a small region near the continental slope in the northern SCS, the beta effect of Coriolis frequency and the influence of background currents were not taken into consideration. The ray tracing model [54,55] is described as

$$\frac{dz}{dy} = \tan\alpha = \sqrt{\frac{\omega^2 - f^2}{N(z)^2 - \omega^2}} \tag{5}$$

where y and z are the local Cartesian coordinates (positive northward and upward, respectively), α is the slope of NIWs, ω, f and $N(z)$ are the NIW, local Coriolis and buoyancy frequencies, respectively. In this study, $N(z)$ was set as the averaged buoyancy frequency near the continental slope along 118° E, f was set to the value of the generation point at the surface and ω was determined through a series of trials. It is found that $\omega = 1.015f$ could lead to reasonable results, therefore, $\omega = 1.015f$ was adopted in the ray tracing model in this study. Figure 8b,d shows the ray tracing results. The two northward–downward-propagating and two southward–downward-propagating beams mentioned above show good consistency with the ray tracing results, confirming the occurrence of reflection of NIWs at the supercritical continental slope in the northern SCS.

Based on the aforementioned analysis, it can be concluded that because the continental slope in the northern SCS is supercritical to Megi-induced NIWs, the NIWs impinging on the continental slope were reflected back and then trapped in the SCS Basin, which finally resulted in the concentrated NIKE in the deep SCS Basin (Figure 6). In addition, because mooring UIB6 was located on the continental slope in the northern SCS, the NIKE here was not very significant. This explains why the strongest typhoon in 2010, Megi, did not generate stronger NIWs than another typhoon, Meranti, at mooring UIB6 [37].

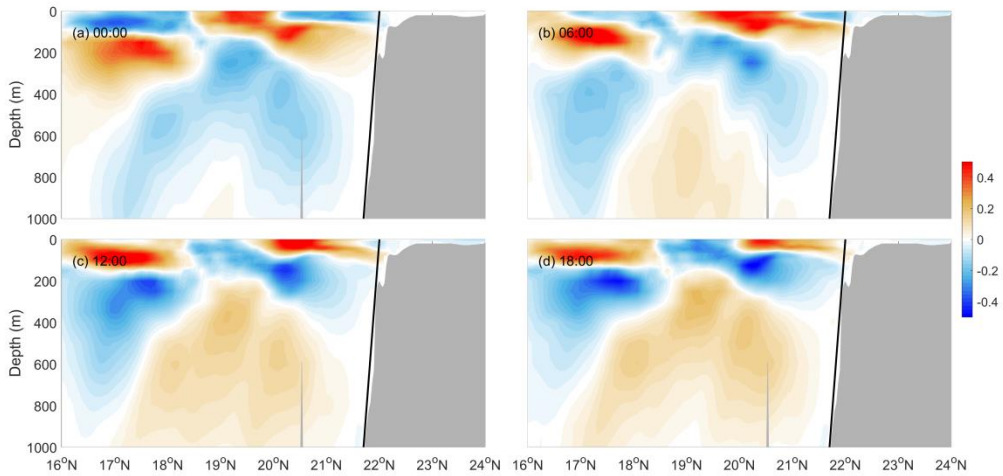

Figure 7. Meridional currents of NIWs (shading, unit: m/s) along 118° E at(**a**) 00:00, (**b**) 06:00, (**c**) 12:00 and (**d**) 18:00 on 24 October. The gray shading in each subfigure indicates the topography. The black solid line in each subfigure indicates the approximate topographic slope.

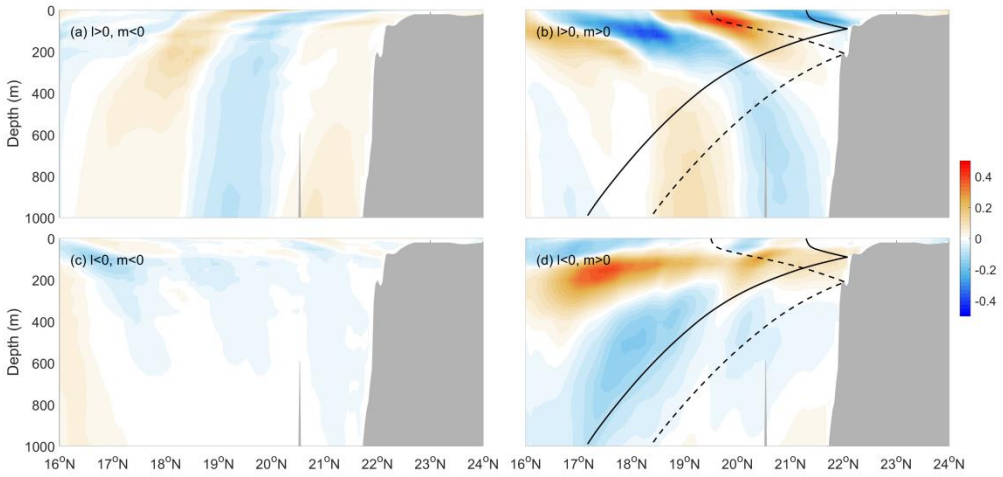

Figure 8. NIWs propagating in different directions along 118° E at 00:00 on 24 October. Note that l and m represent the horizontal and vertical wavenumbers, respectively; $l > 0$ ($l < 0$) corresponds to NIWs propagating northward (southward) and $m < 0$ ($m > 0$) corresponds to NIWs propagating upward (downward). The gray shading in each subfigure indicates the topography. In (**b**,**d**), the black solid and dashed curves represent the ray tracing results.

To study the vertical distribution of Megi-induced NIKE, Figure 9 displays the NIKE at several depths at 00:00 on 24 October as an example. Similar results can be found on the adjacent several days, which are not shown. From Figure 9, we can find that strong NIKE mainly appeared in the upper ocean, especially near the surface. Megi-induced NIKE in the upper 200 m (the upper panels of Figure 9) was at least one order of magnitude stronger than that below 500 m depth (the lower panels of Figure 9). Moreover, there was a slight elevation of NIKE at 1000 m depth, whereas almost no enhancement was found at lower depths. This result suggests that Megi-induced NIWs could only reach an approximate depth of 1000 m in the SCS Basin. In addition, because NIWs are a kind of internal wave which can propagate in both horizontal and vertical directions, the patterns of Megi-induced NIKE at different depths were different.

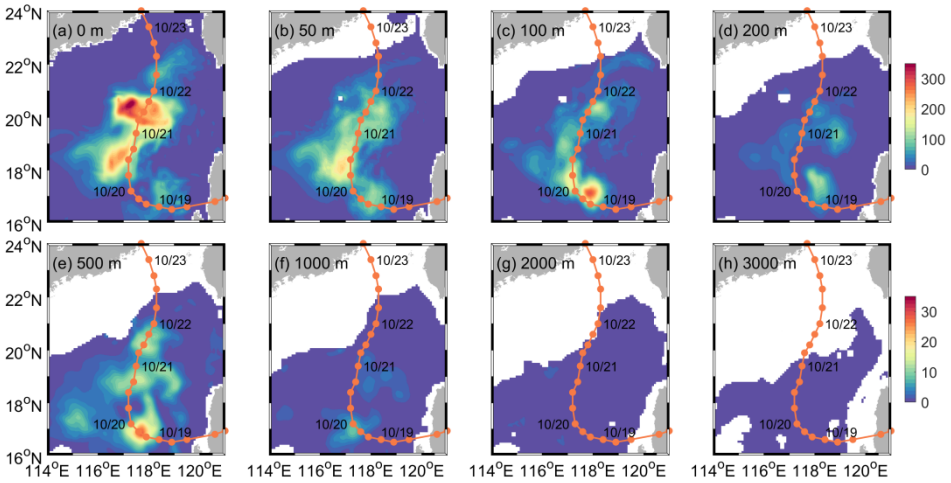

Figure 9. NIKE (shading, unit: J/m^3) at (**a**) 0, (**b**) 50, (**c**) 100, (**d**) 200, (**e**) 500, (**f**) 1000, (**g**) 2000 and (**h**) 3000 m depth at 00:00 on 24 October 2010. Note that the range of colorbar for the upper and lower panels is different. Orange curves denote the track of typhoon Megi.

4.2. Damping

The damping of NIKE is an important characteristic of typhoon-induced NIWs [31,32,34,37]. To investigate the damping of Megi-induced NIWs, Figure 10a illustrates the e-folding time of depth-integrated NIKE. It is interesting to find that the e-folding time of Megi-induced NIWs was site-dependent and varied from several days to approximate a month. Along Megi's track, Megi-induced NIWs damped quickly with the e-folding time generally smaller than one week; whereas away from Megi's track, the e-folding time was longer. It is clearly shown that to the west of Luzon Island and the Luzon Strait, two remarkable zones exist where the e-folding time was longer than 20 days.

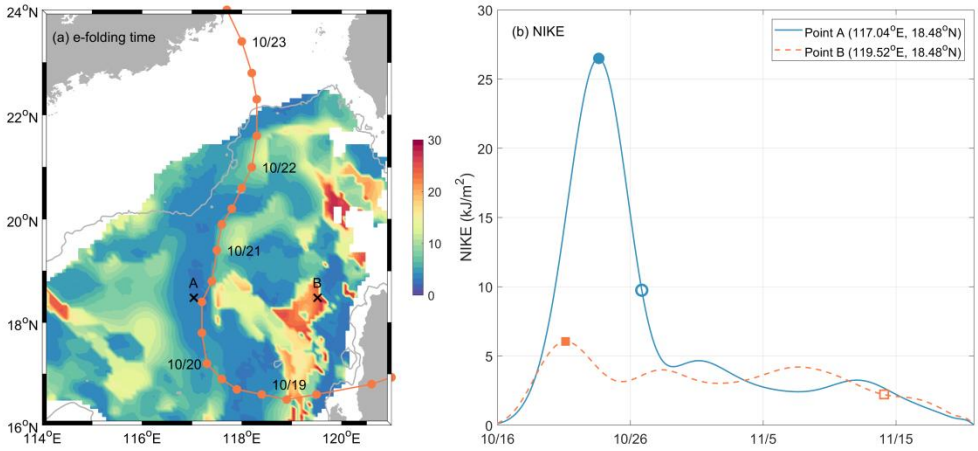

Figure 10. (**a**) The e-folding time (shading, unit: days) of depth-integrated NIKE. The orange curve denotes the track of typhoon Megi. (**b**) Lowpass filtered depth-integrated NIKE at points A (blue solid; 117.04° E, 18.48° N) and B (orange dashed; 119.52° E, 18.48° N) which are marked by black crosses in (**a**). The filled and open circles (squares) locate the maximum and e-folding values of depth-integrated NIKE at point A and B, respectively.

To study the difference of e-folding time along and far away from Megi's track, Figure 10b displays the time series of lowpass filtered depth-integrated NIKE at points A (117.04° E, 18.48° N) and B (119.52° E, 18.48° N) as two examples. At point A which is nearly on Megi's track, the NIKE was quickly strengthened as the response to typhoon Megi, reached the peak value (26.5 kJ/m^2) on 23 October, and quickly damped thereafter.

On 26 October, the NIKE reached the e-folding of its peak value. Therefore, the e-folding time here was 3.1 days. Moreover, the strengthening and damping processes of Megi-induced NIKE at point A were nearly symmetric. However, the situation at point B was much different. First, because point B is far away from Megi's track, the peak value of NIKE was only 6.0 kJ/m^2, which is much smaller than that at point A. Second, the pattern of NIKE evolution here is different from that at point A: Accompanied with the passage of typhoon Megi, the NIKE increased and reached the peak value on 21 October; then the NIKE damped; however, before the NIKE damped to the e-folding of its peak value, it was strengthened again and then exhibited some fluctuations until 7 November. On 14 November, the NIKE at point B reached the e-folding of its peak value. In this case, the e-folding time at point B was 24.0 days.

To explore the possible cause of different damping features of NIKE at points A and B, Figure 11 illustrates the depth-integrated NIKE along the 18.48° N section. As point A is nearly on Megi's track, the NIKE near point A was the strongest along this section. With time going on, the NIKE at point A gradually propagated westward, which is consistent with the result shown in Figure 6. The NIKE at point A damped quickly with significant NIKE existing from 20 to 26 October. As for point B, because it is far away from Megi's track, Megi-induced NIKE here was not significant and only lasted from 19 to 24 October. Thereafter, the NIWs initially generated at 118.8° E propagated eastward to point B and lasted to 1 November, which caused the fluctuations of NIKE at point B (Figure 9c). Similar results can be found at other points with long e-folding time. Based on these results, it can be concluded that the local long damping time of NIKE is related to the NIWs propagating from other sites.

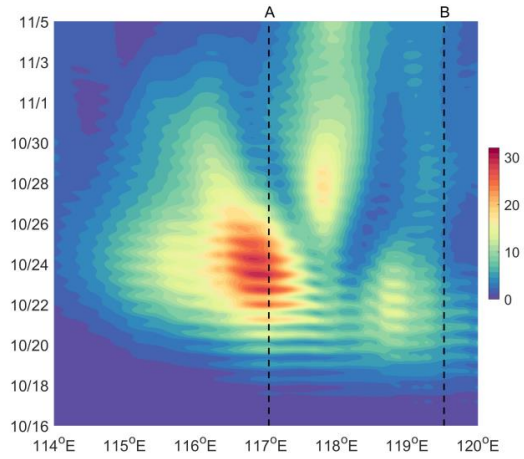

Figure 11. Depth-integrated NIKE (shading, unit: kJ/m^2) as a function of time along 18.48° N. Black dashed lines indicate positions of points A and B.

5. Modal Content

Finally, attention is paid to the modal content of Megi-induced NIWs. We also choose the results at points A and B as examples, for which the modal NIKE is shown in Figure 12. Note that in the modal decomposition in this study, a total of 11 (one barotropic and the first ten baroclinic) modes were taken into consideration.

It is clearly shown that Megi-induced NIWs at point A were dominated by mode-2 which accounted for 45% of the total NIKE. Following mode-2 were mode-3 and mode-1, which occupied 21% and 10% of the total NIKE, respectively. The sum of the first three baroclinic modes accounted for 76% of the total NIKE. The proportions of the other modes in the total NIKE were smaller than 10% and generally exhibited a decreasing trend with the increase in mode number. Moreover, the NIKE of the dominant modes, especially mode-2 and mode-3, synchronously varied with the total NIKE.

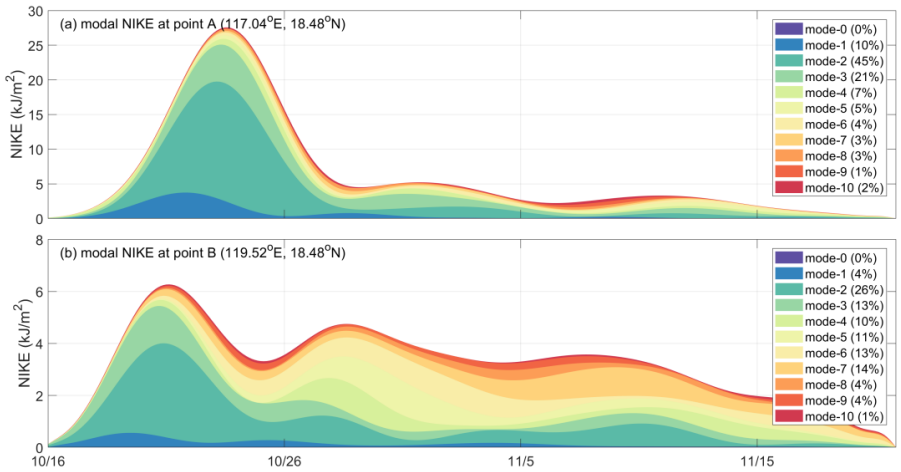

Figure 12. Modal NIKE at points (**a**) A (117.04° E, 18.48° N) and (**b**) B (119.52° E, 18.48° N). The values in the brackets indicate the proportions of modal NIKE in the total NIKE. Note that the modal NIKE has been lowpass filtered to remove oscillations at its own frequency.

The modal content at point B exhibited a different pattern from that at point A. During 16 to 24 October, the locally generated NIWs were dominated by mode-2, mode-3 and mode-1, which was consistent with that at point A; the evolution of mode-2 and mode-3 generally agreed with that of the total NIKE. However, after 24 October, the NIKE of mode-4, mode-5 and mode-6 started to enhance and gradually became dominant. During 5 to 15 November, mode-7 became the most significant mode. On average, mode-2 was the strongest and accounted for 26% of the total NIKE at point B; the contributions of mode-3 to mode-7 were comparable, for which the proportions of modal NIKE in the total NIKE were all greater than 10%.

6. Discussion

The above analysis shows that Megi-induced NIKE was mainly concentrated in the deep SCS basin, which was caused by the reflection of NIWs at the supercritical continental slope around the SCS Basin. A similar phenomenon has been reported for the diurnal internal tides in the SCS [56]. According to the equation of topographic criticality:

$$\gamma = \frac{s_{topo}}{s_{wave}} = \frac{s_{topo}}{\sqrt{(\omega^2 - f^2)/(N^2 - \omega^2)}} \quad (6)$$

where s_{topo} and s_{wave} are the topographic slope and internal wave slope, because the frequency of Megi-induced NIWs (Figure 2) is smaller than that of diurnal internal tides, the s_{wave} for Megi-induced NIWs is smaller than that for diurnal internal tides. In other words, Megi-induced NIWs are more susceptible to reflection on the continental slope in the northern SCS than the diurnal internal tides.

The damping feature of Megi-induced NIWs was site-dependent: In the region near Megi's track, the e-folding time of NIWs was generally less than one week; whereas in two zones to the west of Luzon Island and the Luzon Strait, which are far away from Megi's track, the e-folding time could be longer than 20 days. This result emphasizes the correlation between the distance away from typhoon's track and the decay of NIWs and can partly answer the following questions: Why NIWs generated by different typhoons have different e-folding times at the same position [31] and why NIWs generated by the same typhoon have different e-folding times at different positions [37,57].

The modal decomposition results indicate that Megi-induced NIWs were dominated by the first three baroclinic modes. Along Megi's wake, Megi-induced NIWs quickly dampened after the passage of Megi. However, at point B which is far away from Megi's wake, higher modes (mode-4 to mode-7) appeared and gradually became dominant after

24 October. To explore the possible cause of these higher modes (mode-4 to mode-7), Figure 13 illustrates the zonal currents of NIWs at four points along 18.48° N. By simply counting the times of sign changing of zonal currents in the vertical direction, we can find that these higher modes (mode-4 to mode-7) mainly appeared at point B and 119.04° E, 18.48° N, whereas at point A and 118° E, 18.48° N, these higher modes are nearly invisible. In other words, the appearance of these higher modes (mode-4 to mode-7) was limited to a small region near point B. According to [58], higher modes can be generated when low-mode internal waves interact with mesoscale eddies. Figure 14 illustrates the HYCOM surface elevations from 18 October to 1 November with an interval of 2 days. From Figure 14, we can find that an anticyclonic eddy formed around 24 October and influenced the region around point B. As mentioned above, the NIWs initially generated at 118.8° E propagated eastward to point B after 24 October (Figure 11). This case is similar to that reported by [58]. Therefore, we speculated that the higher modes (mode-4 to mode-7) at point B after 24 October were likely caused by the interaction between NIWs and a mesoscale eddy. However, point A was also under the influence of a cyclonic eddy after 22 October. Why higher modes (mode-4 to mode-7) did not become significant at point A remains unclear. Therefore, the difference of modal content at points A and B still needs further exploration.

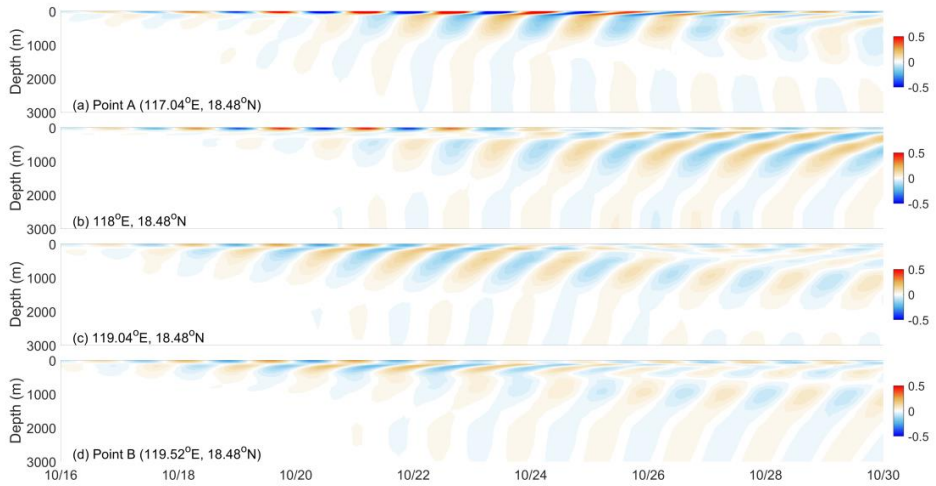

Figure 13. Zonal currents of NIWs (shading, unit: m/s) at (**a**) point A (117.04° E, 18.48° N), (**b**) 118° E, 18.48° N, (**c**) 119.04° E, 18.48° N and (**d**) point B (119.52° E, 18.48° N) from 16 to 30 October 2010.

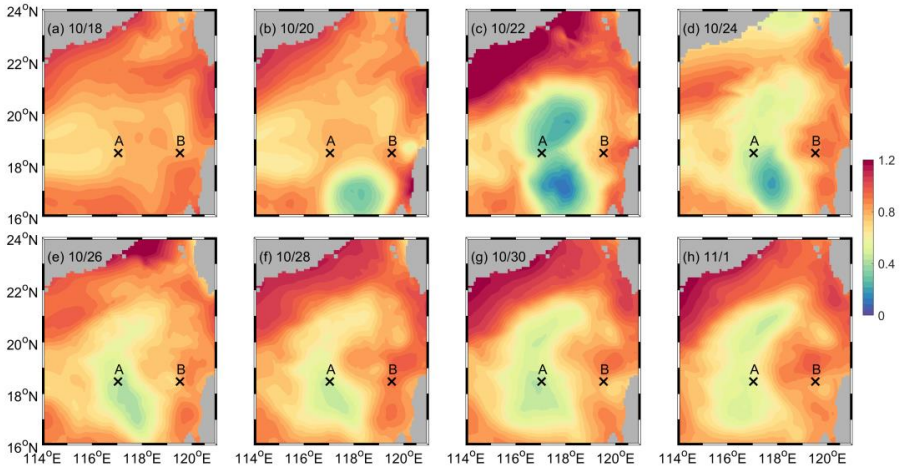

Figure 14. HYCOM surface elevations (shading, unit: m) at 00:00 on (**a**) 18, (**b**) 20, (**c**) 22, (**d**) 24, (**e**) 26, (**f**) 28 and (**g**) 30 October and (**h**) 1 November 2010.

7. Conclusions

Based on the HYCOM reanalysis results, the NIWs generated by typhoon Megi in 2010 in the SCS were investigated in this study. Through a comparison with in situ observations at mooring UIB6, we first showed that the HYCOM reanalysis results can reasonably reproduce typhoon-induced NIWs, which can act as a supplement to in situ observations and provide us with an opportunity to better understand NIWs.

The results indicate that Megi-induced NIWs showed temporal and spatial variations in the SCS. The NIKE in the SCS was rapidly enhancedin response to typhoon Megi. However, the strongest NIKE appeared several days after the passage of Megi, rather than under its influence. Moreover, it is interesting to note that Megi-induced NIKE was mainly concentrated in the deep SCS basin where the water depth is greater than 1000 m, although typhoon Megi passed over both the deep SCS basin and shallow continental shelf and slope in the northern SCS. Through analysis, it was found that the continental slope in the northern SCS is supercritical to Megi-induced NIWs. In other words, when Megi-induced NIWs impinged on the continental slope, they were reflected and trapped in the deep SCS basin. This conclusion was validated by comparing the northward–downward and southward–downward components of Megi-induced NIWs. Moreover, it is found that Megi-induced NIWs could reach 1000 m depth in the vertical direction.

In situ observations have shown that Megi-induced NIWs dampened quickly at mooring UIB6 [32,37]. However, the HYCOM reanalysis results indicate that only in the region near Megi's track did the NIWs exhibit a similar feature, with the e-folding time generally being smaller than one week; whereas in two zones to the west of Luzon Island and the Luzon Strait, which are far away from Megi's track, the e-folding time of Megi-induced NIWs could be longer than 20 days. It was found that the NIWs generated at other sites could propagate to the two zones and influence the local NIKE, which accounted for the long e-folding time.

The modal content of Megi-induced NIWs was also explored in this study. Near Megi's track, Megi-induced NIWs were dominated by mode-2, which was followed by mode-3 and mode-1. The three modes accounted for 76% of the total NIKE. However, at the region far away from Megi's track, the NIKE of higher modes (mode-4 to mode-7) was enhanced several days after the passage of typhoon Megi. The cause of these higher modes still needs further exploration.

Author Contributions: Conceptualization, A.C.; methodology, A.C. and Z.G.; formal analysis, A.C., Z.G. and Y.P.; writing—original draft preparation, A.C.; writing—review and editing, A.C., Z.G., J.S., H.H. and P.L.; supervision, A.C. and J.S.; funding acquisition, A.C. and H.H. All authors have read and agreed to the published version of the manuscript.

Funding: This research was funded by the Natural Science Foundation of Zhejiang Province through grant LY21D060005, the Joint Project of Zhoushan Municipality and Zhejiang University through grant 2019C81060, and the National Natural Science Foundation of China through grant 41621064. This research was also supported by the Laboratory for Regional Oceanography and Numerical Modeling, Qingdao National Laboratory for Marine Science and Technology through grant 2019A01.

Conflicts of Interest: The authors declare no conflict of interest.

References

1. Alford, M.H.; MacKinnon, J.A.; Simmons, H.L.; Nash, J.D. Near-Inertial Internal Gravity Waves in the Ocean. *Annu. Rev. Mar. Sci.* **2016**, *8*, 95–123. [CrossRef]
2. Garrett, C. Mixing with latitude. *Nat. Cell Biol.* **2003**, *422*, 477. [CrossRef] [PubMed]
3. Carter, G.; Fringer, O.; Zaron, E. Regional Models of Internal Tides. *Oceanography* **2012**, *25*, 56–65. [CrossRef]
4. Zhang, Z.; Qiu, B.; Tian, J.; Zhao, W.; Huang, X. Latitude-dependent finescale turbulent shear generations in the Pacific trop-ical-extratropical upper ocean. *Nat. Commun.* **2018**, *9*, 4086. [CrossRef] [PubMed]
5. Cao, A.; Guo, Z.; Wang, S.; Chen, X.; Lv, X.; Song, J. Upper ocean shear in the northern South China Sea. *J. Oceanogr.* **2019**, *75*, 525–539. [CrossRef]
6. Jing, Z.; Wu, L. Low-Frequency Modulation of Turbulent Diapycnal Mixing by Anticyclonic Eddies Inferred from the HOT Time Series. *J. Phys. Oceanogr.* **2013**, *43*, 824–835. [CrossRef]

7. Whalen, C.B.; MacKinnon, J.A.; Talley, L.D. Large-scale impacts of the mesoscale environment on mixing from wind-driven internal waves. *Nat. Geosci.* **2018**, *11*, 842–847. [CrossRef]
8. Alford, M.H. Internal Swell Generation: The Spatial Distribution of Energy Flux from the Wind to Mixed Layer Near-Inertial Motions. *J. Phys. Oceanogr.* **2001**, *31*, 2359–2368. [CrossRef]
9. Alford, M.H. Improved global maps and 54-year history of wind-work on ocean inertial motions. *Geophys. Res. Lett.* **2003**, *30*, 1424. [CrossRef]
10. Watanabe, M.; Hibiya, T. Global estimates of the wind-induced energy flux to inertial motions in the surface mixed layer. *Geophys. Res. Lett.* **2002**, *29*, 64-1–64-3. [CrossRef]
11. Furuichi, N.; Hibiya, T.; Niwa, Y. Model-predicted distribution of wind-induced internal wave energy in the world's oceans. *J. Geophys. Res. Oceans* **2008**, *113*, C09034. [CrossRef]
12. Jiang, J.; Lu, Y.; Perrie, W. Estimating the energy flux from the wind to ocean inertial motions: The sensitivity to surface wind fields. *Geophys. Res. Lett.* **2005**, *32*, 291–310. [CrossRef]
13. Rimac, A.; Storch, J.; Eden, C.; Haak, H. The influence of high-resolution wind stress field on the power input to near-inertial motions in the ocean. *Geophys. Res. Lett.* **2013**, *40*, 4882–4886. [CrossRef]
14. Simmons, H.; Alford, M. Simulating the Long-Range Swell of Internal Waves Generated by Ocean Storms. *Oceanography* **2012**, *25*, 30–41. [CrossRef]
15. Munk, W.; Wunsch, C. Abyssal recipes II: Energetics of tidal and wind mixing. *Deep. Sea Res. Part I Oceanogr. Res. Pap.* **1998**, *45*, 1977–2010. [CrossRef]
16. Egbert, G.D.; Ray, R.D. Significant dissipation of tidal energy in the deep ocean inferred from satellite altimeter data. *Nat. Cell Biol.* **2000**, *405*, 775–778. [CrossRef]
17. Alford, M.H.; MacKinnon, J.A.; Zhao, Z.; Pinkel, R.; Klymak, J.; Peacock, T. Internal waves across the Pacific. *Geophys. Res. Lett.* **2007**, *34*, 24601. [CrossRef]
18. Xie, X.-H.; Shang, X.-D.; Chen, G.-Y.; Sun, L. Variations of diurnal and inertial spectral peaks near the bi-diurnal critical latitude. *Geophys. Res. Lett.* **2009**, *36*, 02606. [CrossRef]
19. MacKinnon, J.A.; Alford, M.H.; Sun, O.; Pinkel, R.; Zhao, Z.; Klymak, J. Parametric Subharmonic Instability of the Internal Tide at 29° N. *J. Phys. Oceanogr.* **2013**, *43*, 17–28. [CrossRef]
20. Nikurashin, M.; Legg, S. A Mechanism for Local Dissipation of Internal Tides Generated at Rough Topography. *J. Phys. Oceanogr.* **2011**, *41*, 378–395. [CrossRef]
21. Liang, X.; Wunsch, C. Note on the redistribution and dissipation of tidal energy over mid-ocean ridges. *Tellus A Dyn. Meteorol. Oceanogr.* **2015**, *67*, 27385. [CrossRef]
22. Wang, S.; Cao, A.; Chen, X.; Li, Q.; Song, J. On the resonant triad interaction over mid-ocean ridges. *Ocean. Model.* **2021**, *158*, 101734. [CrossRef]
23. Nikurashin, M.; Ferrari, R. Radiation and dissipation of internal waves generated by geostrophic gotions impinging on small-scale topography: Theory. *J. PhysOceanogr.* **2010**, *40*, 2025–2042.
24. Alford, M.H.; Shcherbina, A.Y.; Gregg, M.C. Observations of Near-Inertial Internal Gravity Waves Radiating from a Frontal Jet. *J. Phys. Oceanogr.* **2013**, *43*, 1225–1239. [CrossRef]
25. Liang, X.; Thurnherr, A.M. Eddy-Modulated Internal Waves and Mixing on a Midocean Ridge. *J. Phys. Oceanogr.* **2012**, *42*, 1242–1248. [CrossRef]
26. D'Asaro, E.; Black, P.; Centurioni, L.; Harr, P.; Jayne, S.; Lin, I.; Lee, C.; Morzel, J.; Mrvaljevic, R.; Niiler, P.; et al. Typhoon-Ocean Interaction in the Western North Pacific: Part 1. *Oceanography* **2011**, *24*, 24–31. [CrossRef]
27. Nguyen, C.H.; Owen, J.S.; Franke, J.; Neves, L.C.; Hargreaves, D.M. Typhoon track simulations in the North West Pacific: Informing a new wind map for Vietnam. *J. Wind. Eng. Ind. Aerodyn.* **2021**, *208*, 104441. [CrossRef]
28. Wang, L.; Li, J.; Lizhen, W.; Jiachun, L. Estimation of extreme wind speed in SCS and NWP by a non-stationary model. *Theor. Appl. Mech. Lett.* **2016**, *6*, 131–138. [CrossRef]
29. Li, J.; Xu, J.; Liu, J.; He, Y.; Chen, Z.; Cai, S. Correlation of Near-Inertial Wind Stress in Typhoon and Typhoon-Induced Oceanic Near-Inertial Kinetic Energy in the Upper South China Sea. *Atmosphere* **2019**, *10*, 388. [CrossRef]
30. Sun, Z.; Hu, J.; Zheng, Q.; Li, C. Strong near-inertial oscillations in geostrophic shear in the northern South China Sea. *J. Oceanogr.* **2011**, *67*, 377–384. [CrossRef]
31. Chen, G.; Xue, H.; Wang, D.; Xie, Q. Observed near-inertial kinetic energy in the northwestern South China Sea. *J. Geophys. Res. Oceans* **2013**, *118*, 4965–4977. [CrossRef]
32. Guan, S.; Zhao, W.; Huthnance, J.; Tian, J.; Wang, J. Observed upper ocean response to typhoon Megi (2010) in the Northern South China Sea. *J. Geophys. Res. Oceans* **2014**, *119*, 3134–3157. [CrossRef]
33. Yang, B.; Hou, Y. Near-inertial waves in the wake of 2011 Typhoon Nesat in the northern South China Sea. *Acta Oceanol. Sin.* **2014**, *33*, 102–111. [CrossRef]
34. Yang, B.; Hou, Y.; Hu, P.; Liu, Z.; Liu, Y. Shallow ocean response to tropical cyclones observed on the continental shelf of the northwestern South China Sea. *J. Geophys. Res. Oceans* **2015**, *120*, 3817–3836. [CrossRef]
35. Zhang, H.; Chen, D.; Zhou, L.; Liu, X.; Ding, T.; Zhou, B. Upper ocean response to typhoon Kalmaegi (2014). *J. Geophys. Res. Oceans* **2016**, *121*, 6520–6535. [CrossRef]

36. Zhang, H.; Wu, R.; Chen, D.; Liu, X.; He, H.; Tang, Y.; Ke, D.; Shen, Z.; Li, J.; Xie, J.; et al. Net Modulation of Upper Ocean Thermal Structure by Typhoon Kalmaegi (2014). *J. Geophys. Res. Oceans* **2018**, *123*, 7154–7171. [CrossRef]
37. Cao, A.; Guo, Z.; Song, J.; Lv, X.; He, H.; Fan, W. Near-Inertial Waves and Their Underlying Mechanisms Based on the South China Sea Internal Wave Experiment (2010–2011). *J. Geophys. Res. Oceans* **2018**, *123*, 5026–5040. [CrossRef]
38. Ding, W.; Liang, C.; Liao, G.; Li, J.; Lin, F.; Jin, W.; Zhu, L. Propagation characteristics of near-inertial waves along the conti-nental shelf in the wake of the 2008 Typhoon Hagupit in the northern South China Sea. *B. Mar. Sci.* **2018**, *94*, 1293–1311. [CrossRef]
39. Ma, Y.; Zhang, S.; Qi, Y.; Jing, Z. Upper ocean near-inertial response to the passage of two sequential typhoons in the north-western South China Sea. *Sci. China Earth Sci.* **2019**, *62*, 863–871. [CrossRef]
40. Xu, J.; Huang, Y.; Chen, Z.; Liu, J.; Liu, T.; Li, J.; Cai, S.; Ning, D. Horizontal variations of typhoon-forced near-inertial oscillations in the south China sea simulated by a numerical model. *Cont. Shelf Res.* **2019**, *180*, 24–34. [CrossRef]
41. Ying, M.; Zhang, W.; Yu, H.; Lu, X.; Feng, J.; Fan, Y.; Zhu, Y.; Chen, D. An Overview of the China Meteorological Administration Tropical Cyclone Database. *J. Atmos. Ocean. Technol.* **2014**, *31*, 287–301. [CrossRef]
42. Mercier, M.J.; Garnier, N.B.; Dauxois, T. Reflexion and Diffraction of Internal Waves analyzed with the Hilbert Transform. *Phys. Fluids* **2008**, *20*, 086601. [CrossRef]
43. Wang, S.; Cao, A.; Chen, X.; Li, Q.; Song, J.; Meng, J. Estimation of the Reflection of Internal Tides on a Slope. *J. Ocean. Univ. China* **2020**, *19*, 489–496. [CrossRef]
44. Nash, J.D.; Alford, M.H.; Kunze, E. Estimating Internal Wave Energy Fluxes in the Ocean. *J. Atmos. Ocean. Technol.* **2005**, *22*, 1551–1570. [CrossRef]
45. Zhao, Z.; Alford, M.H.; Mackinnon, J.A.; Pinkel, R. Long-Range Propagation of the Semidiurnal Internal Tide from the Ha-waiian Ridge. *J. Phys. Oceanogr.* **2010**, *40*, 713–736. [CrossRef]
46. Cao, A.-Z.; Li, B.-T.; Lv, X.-Q. Extraction of Internal Tidal Currents and Reconstruction of Full-Depth Tidal Currents from Mooring Observations. *J. Atmos. Ocean. Technol.* **2015**, *32*, 1414–1424. [CrossRef]
47. Shang, X.; Liu, Q.; Xie, X.; Chen, G.; Chen, R. Characteristics and seasonal variability of internal tides in the southern South China Sea. *Deep. Sea Res. Part I Oceanogr. Res. Pap.* **2015**, *98*, 43–52. [CrossRef]
48. Zhao, Z.; Alford, M.H.; Lien, R.-C.; Gregg, M.C.; Carter, G.S. Internal Tides and Mixing in a Submarine Canyon with Time-Varying Stratification. *J. Phys. Oceanogr.* **2012**, *42*, 2121–2142. [CrossRef]
49. D'Asaro, E.A.; Eriksen, C.C.; Levine, M.D.; Niiler, P.; Paulson, C.A.; Meurs, P.V. Upper-ocean inertial currents forced by a strong storm. Part I: Data and comparisons with linear theory. *J. Phys. Oceanogr.* **1995**, *25*, 2909–2936. [CrossRef]
50. Gill, A.E. On the Behavior of Internal Waves in the Wakes of Storms. *J. Phys. Oceanogr.* **1984**, *14*, 1129–1151. [CrossRef]
51. Sun, O.M.; Pinkel, R. Energy Transfer from High-Shear, Low-Frequency Internal Waves to High-Frequency Waves near Kaena Ridge, Hawaii. *J. Phys. Oceanogr.* **2012**, *42*, 1524–1547. [CrossRef]
52. Guo, Z.; Cao, A.; Lv, X.; Song, J. Impact of multiple tidal forcing on the simulation of the M2 internal tides in the northern South China Sea. *Ocean.Dyn.* **2019**, *70*, 187–198. [CrossRef]
53. Price, J.F.; Sanford, T.B.; Forristall, G.Z. Forced Stage Response to a Moving Hurricane. *J. Phys. Oceanogr.* **1994**, *24*, 233–260. [CrossRef]
54. Cacchione, D.A.; Pratson, L.F.; Ogston, A.S. The shaping of continental slopes by internal tides. *Science* **2020**, *296*, 724–727. [CrossRef] [PubMed]
55. Guo, Z.; Cao, A.; Lv, X.; Song, J. Impacts of Stratification Variation on the M2 Internal Tide Generation in Luzon Strait. *Atmos. Ocean.* **2020**, *58*, 206–218. [CrossRef]
56. Wu, L.; Miao, C.; Zhao, W. Patterns of K1 and M2 internal tides and their seasonal variations in the northern South China Sea. *J. Oceanogr.* **2013**, *69*, 481–494. [CrossRef]
57. Hu, S.; Liu, L.; Guan, C.; Zhang, L.; Hu, D. Dynamic features of near-inertial oscillations in the Northwest Pacific derived from mooring observations from 2015 to 2018. *J. Oceanol. Limn.* **2020**, *38*, 1092–1107. [CrossRef]
58. Dunphy, M.; Lamb, K.G. Focusing and vertical mode scattering of the first mode internal tide by mesoscale eddy interaction. *J. Geophys. Res. Oceans* **2014**, *119*, 523–536. [CrossRef]